Supporting Information

Experimental and DFT Study of Electrochemical Promotion of Cu/ZnO Catalysts for the Reverse Water Gas Shift Reaction

Ju Wang[†], Mario G. Sandoval[‡], Martin Couillard[§], Estela A. González[‡], Paula V. Jasen[‡], Alfredo Juan[‡], Arnaud Weck[#] and Elena A. Baranova[,†]*

[†]Department of Chemical and Biological Engineering, Centre for Catalysis Research and Innovation (CCRI), Nexus for Quantum Technologies (NexQT), University of Ottawa, Ottawa, K1N 6N5, Canada.

[‡]Instituto de Física del Sur (IFISUR), Departamento de Física, Universidad Nacional del Sur (UNS), CONICET, Av. L. N. Alem 1253, Bahía Blanca, B8000CPB, Argentina.

[§]National Research Council of Canada, 1200 Montreal Road, Ottawa, K1A 0R6, Canada.

[#]Department of Mechanical Engineering, Nexus for Quantum Technologies (NexQT), University of Ottawa, Ottawa, K1N 6N5, Canada.

[*]Corresponding Author: E-mail: Elena.baranova@uottawa.ca

Number of pages: 22 pages

Number of Figures: 13 Figures

Number of Tables: 6 Tables

Detailed Computational Methodology. The bulk of wurtzite ZnO were simulated using the $p6\bar{3}mc$ space group.[1] The obtained lattice parameters of a = b = 3.166 Å, c/a = 1.611 Å (c = 5.102 Å) and α = β = 90°, γ = 60° are in good agreement with reported experimental and theoretical values.[2,3] As shown in Figure S1, the ZnO (101) low-index surface was modeled as a super-cell with five ZnO bilayers along the vacuum direction and 4 × 4 primitive cell on the in-plane direction. This ZnO plane was chosen based on experimental information in Section 2.1. The 15 Å vacuum layer on top (z-direction) was enough to prevent interactions between periodic images of the slabs. In the optimization of the surfaces, the three outmost layers on the top were relaxed, while the two bottom layers were frozen in the relaxed bulk positions.

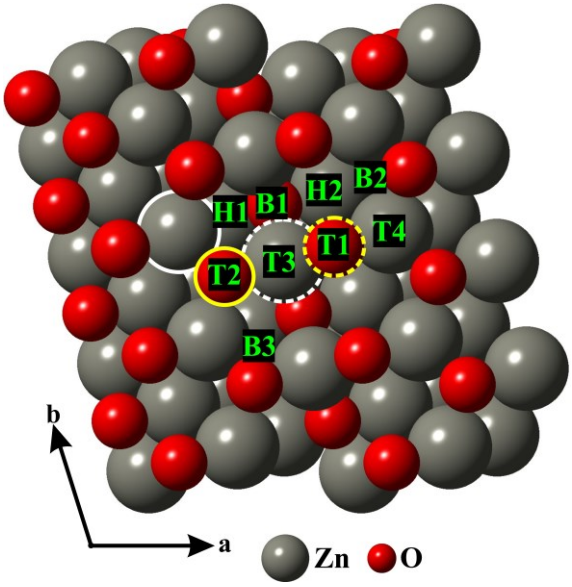

Figure S1. Schematic view of high symmetrical possible adsorption sites on the ZnO (101) surface. The B1, B2, and B3 indicate the Zn-Zn bridge sites with different chemical environments. The H1 and H2 represent the hollow sites. The T1 and T2 labels show the Top sites on the O atoms, while the T3 and T4 are the Top sites on Zn atoms. The Zn and O highlighted atoms are those chosen to generate the different types of vacancies. The white and yellow full (V_{Zn1} or V_{O1}) and dotted (V_{Zn2} or V_{O2}) lines correspond to Zn and O vacancies.

The different high symmetrical adsorption sites that were considered to study the interaction of a Cu-atom with the surface are presented in Figure S1. For a more realistic representation, a second Cu atom was adsorbed at the nearest and the most energetically favorable adsorption site. Then an O-atom was adsorbed along the high symmetrical adsorption sites surrounding the Cu-atom and the two Cu-atoms for both considered systems.

To assess the difficulty of vacancy formation, O and Zn vacancies were generated in the outmost layer by simply removing an atom. The specific atoms chosen for removal are also indicated in Figure S1. In an effort to elucidate the potential mechanism of copper oxide formation during the electrooxidation process, the extraction of oxygen from the most stable O-vacancy locations was simulated by incrementally moving it in 0.1 Å steps upward on the ZnO surface with two adsorbed Cu-atoms.

The adsorption energies, represented as E_{ads} in eV, were computed as the difference between the total energy of the system after adsorption ($E_{adsorbate/substrate}$) and the energy of the isolated atom in a box ($E_{adsorbate}$) plus the energy of the clean surface ($E_{substrate}$). This calculation is expressed in Equation (S1):

$$\mathrm{E_{ads}} = \mathrm{E_{adsorbate/substrate}} - (\mathrm{E_{adsorbate}} + \mathrm{E_{substrate}}) \quad \text{(S1)}$$

For the E_{ads}, a smaller value signifies a more favourable adsorption site and a positive value indicates an endothermic reaction, while a negative one suggests an exothermic process. In this case, the oxygen is considered as coming after the entire process of CO_2 electrochemical reduction to CO, where the final products are primarily CO(g) and O^*.[4] Then the $E_{adsorbate}$ is calculated from an atomic oxygen isolated in a box.

The energy barrier (E_{bar}), reaction energy (E_r), and reverse energy barrier (E_{rbar}) are calculated in Equation (S2-4):

$$\mathrm{E_{bar}} = \mathrm{E_{TS}} - \mathrm{E_{IS}} \quad \text{(S2)}$$

$$\mathrm{E_{r}} = \mathrm{E_{FS}} - \mathrm{E_{IS}} \quad \text{(S3)}$$

$$\mathrm{E_{rbar}} = \mathrm{E_{TS}} - \mathrm{E_{FS}} \quad \text{(S4)}$$

where E_{IS}, E_{FS} and E_{TS} refer to the initial-, final- and transition-state energies. The vacancy formation energy (E_{vac}) is computed at zero kelvin in Equation (S5) (a lower value indicates a more energetically favorable condition):

$$\mathrm{E_{vac}} = \left(\mathrm{E_{ZnO(101)+vac}} + \mathrm{E_{vac-atom}}\right) - \mathrm{E_{ZnO(101)}} \quad \text{(S5)}$$

where $E_{ZnO(101)+vac}$ is the total energy of the system in the presence of the defect, $E_{vac\text{-}atom}$ is the energy of the isolated atom deleted from the vacancy and $E_{ZnO(101)}$ is the total energy of the system without any vacancy.[5]

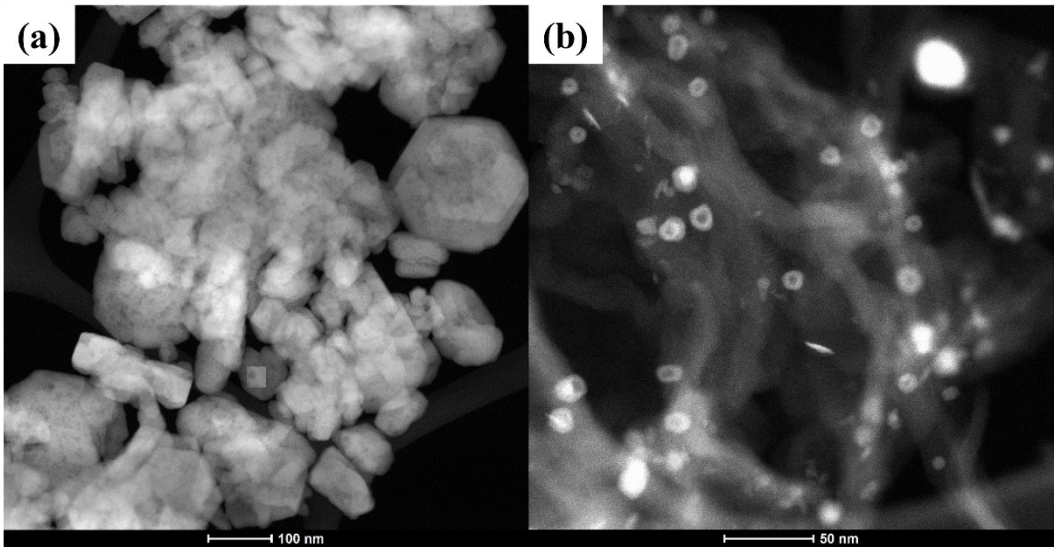

Figure S2. HAADF-STEM image of (a) bare ZnO and (b) unsupported Cu NPs.

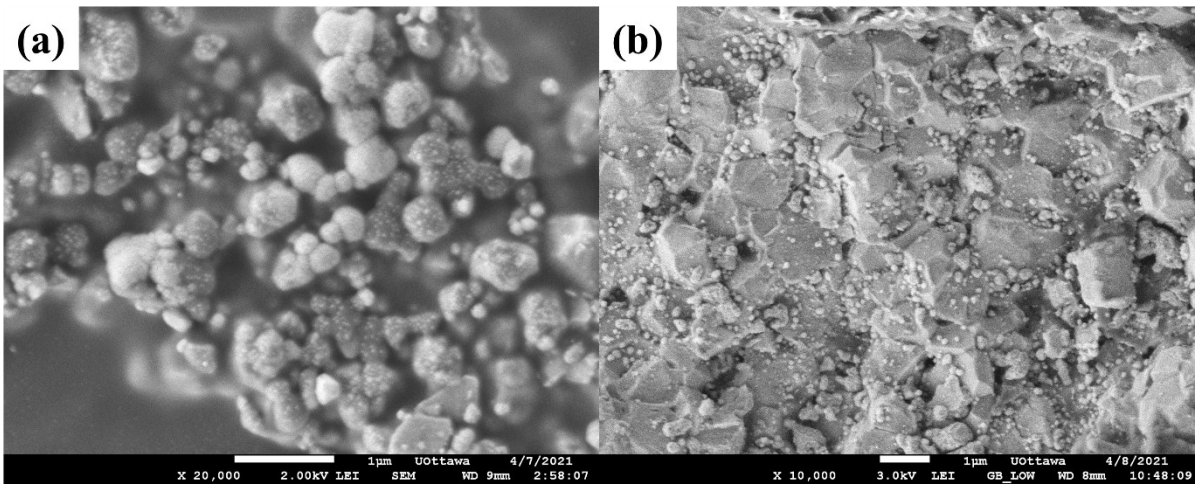

Figure S3. SEM images of (a) as-prepared and (b) spent unsupported Cu NPs deposited on YSZ on scale of 1 µm.

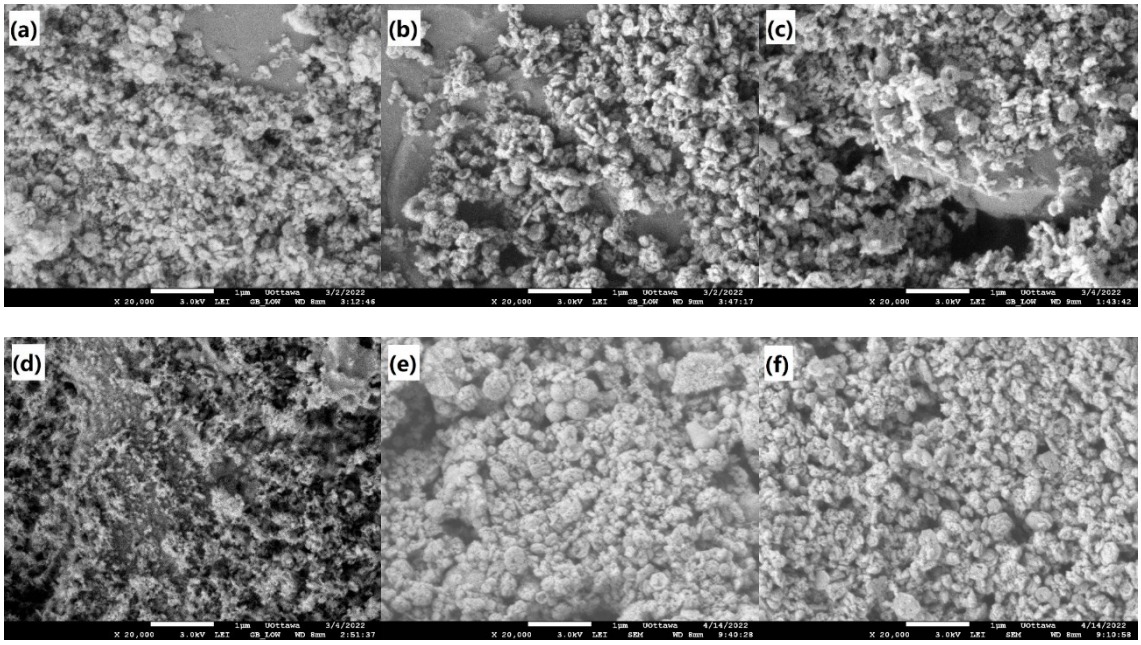

Figure S4. SEM images of spent (a) ZnO, and (b) 5wt.%, (c) 10wt.%, (d) 20wt.%, (e) 40wt.%, and (f) 60wt.%Cu supported on ZnO on the scale of 1 μm.

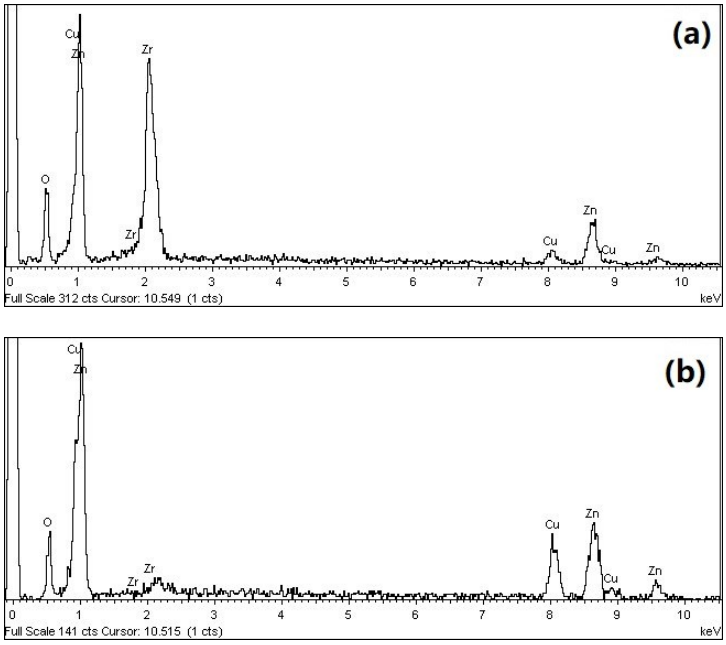

Figure S5. EDS spectrums of (a) 10CuZnO and (b) 60CuZnO.

Table S1. Summary of major peak positions and corresponding interplanar distances (d), full width at half maximum (FWHM) and crystallite sizes (L). n=1, λ=0.15418 nm, and K=0.9.

ZnO									
	as-prepared					spent			
	2θ	d (nm)	FWHM (rad)	size (nm)		2θ	d (nm)	FWHM (rad)	size (nm)
ZnO (101)	36.16	0.248	0.00577703	25.26718	ZnO (101)	36.18	0.248	0.00551524	26.46807
Cu (111)	N/A	N/A	N/A	N/A	Cu (111)	N/A	N/A	N/A	N/A
Cu_2O (110)	N/A	N/A	N/A	N/A	Cu_2O (110)	N/A	N/A	N/A	N/A
10CuZnO									
	as-prepared					spent			
	2θ	d (nm)	FWHM (rad)	size (nm)		2θ	d (nm)	FWHM (rad)	size (nm)
ZnO (101)	36.18	0.248	0.00678933	21.50106	ZnO (101)	36.18	0.248	0.00532325	27.42266
Cu (111)	43.28	0.209	0.00432841	34.48922	Cu (111)	43.22	0.209	0.00376991	39.59052
Cu_2O (110)	N/A	N/A	N/A	N/A	Cu_2O (110)	30.02	0.297	0.00371755	38.64475
60CuZnO									
	as-prepared					spent			
	2θ	d (nm)	FWHM (rad)	size (nm)		2θ	d (nm)	FWHM (rad)	size (nm)
ZnO (101)	36.18	0.248	0.0056025	26.0558	ZnO (101)	36.16	0.248	0.00574213	25.42077
Cu (111)	43.22	0.209	0.00446804	33.4045	Cu (111)	43.22	0.209	0.00401425	37.18066
Cu_2O (110)	N/A	N/A	N/A	N/A	Cu_2O (110)	29.98	0.297	0.00438077	32.79108

The Scherrer equation and Bragg equation are used to determine the crystallite sizes of NPs and interplanar distances. The calculations are shown in Equation S6 and S7, respectively:

$$L = K\lambda/FWHM \cdot \cos\theta \quad \text{(S6)}$$

$$n\lambda = 2d \cdot \sin\theta \quad \text{(S7)}$$

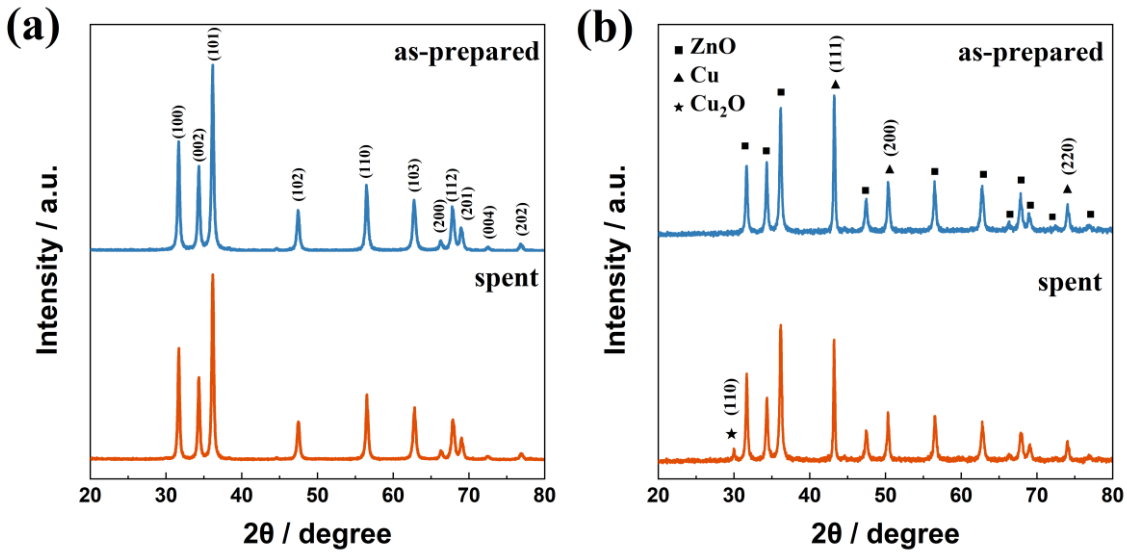

Figure S6. XRD patterns of as-prepared and spent (a) bare ZnO and (b) 60CuZnO.

Table S2. XPS data of Cu 2p for as-prepared and spent 10CuZnO.

Element	Composition	Position (eV)		FWHM		%Area	
		as-prepared	spent	as-prepared	spent	as-prepared	spent
Cu $2p_{1/2}$	N/A	951.3	951.3	N/A	N/A	N/A	N/A
Cu $2p_{3/2}$	Cu^0	931.5	931.5	1.60	1.68	67.62	53.26
	Cu^{1+}	931.3	931.2	0.78	1.09	12.93	27.54
	Cu^{2+}	933.5	933.4	2.01	2.49	19.45	19.20

Table S3. XPS data of Zn 2p and O1s for as-prepared ZnO, 10CuZnO and 60CuZnO.

Catalyst	Element	Composition	Position (eV)	FWHM	%Area
ZnO	O 1s	O_L	530.25	1.103	44.19
		O_V	531.02	1.969	48.58
		-OH	532.26	1.41	7.23
	Zn 2p	$Zn\ 2p_{1/2}$	1044.05	N/A	N/A
		$Zn\ 2p_{3/2}$	1021.03	N/A	N/A
10CuZnO	O 1s	O_L	530.29	1.007	50.29
		O_V	531.08	1.942	44.43
		-OH	532.19	1.242	5.28
	Zn 2p	$Zn\ 2p_{1/2}$	1044.45	N/A	N/A
		$Zn\ 2p_{3/2}$	1021.43	N/A	N/A
60CuZnO	O 1s	O_L	530.8	1.063	64.23
		O_V	531.64	1.394	21.47
		-OH	532.74	1.318	14.3
	Zn 2p	$Zn\ 2p_{1/2}$	1045.26	N/A	N/A
		$Zn\ 2p_{3/2}$	1022.13	N/A	N/A

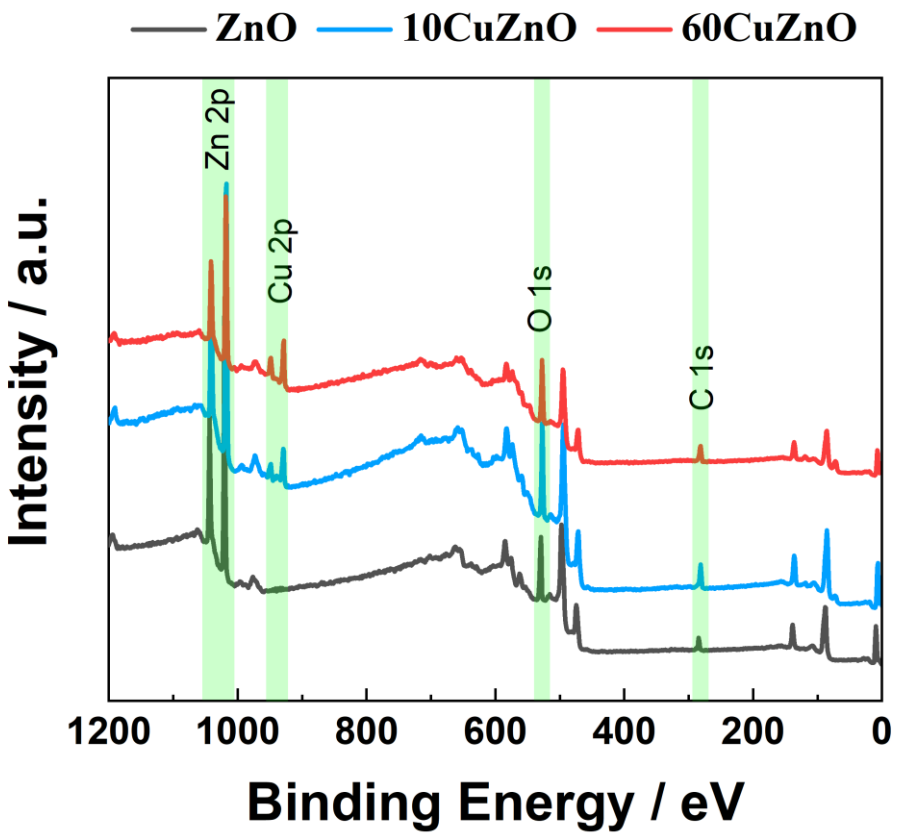

Figure S7. Wide scan XPS spectra of as-prepared ZnO, 10CuZnO and 60CuZnO.

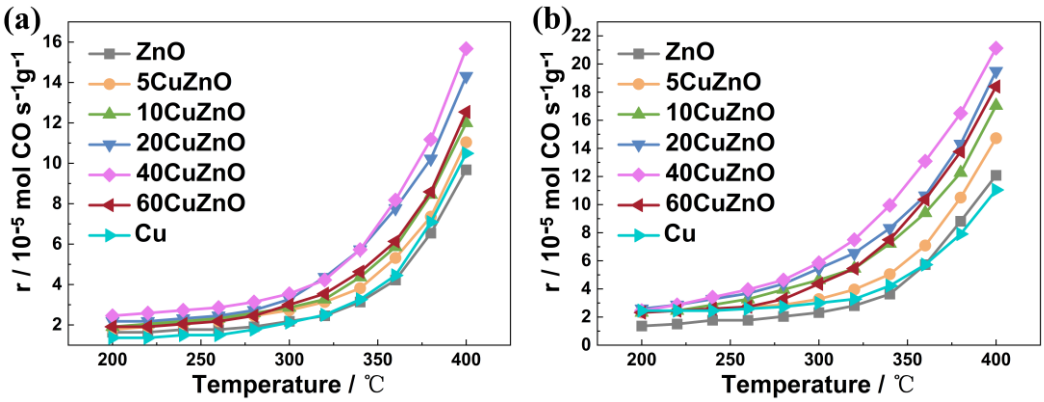

Figure S8. Light-off curves for all Cu/ZnO catalysts under (a) oxidizing and (b) reducing conditions.

The dispersion (D) of Cu/ZnO nanoparticles is calculated from Equation (S8):[6]

$$D = 6 \times \frac{V/A}{d_{TEM}} \quad (S8)$$

where V and A represent the volume and surface area of a Cu atom and d_{TEM} is the particle size of Cu according to the TEM image. The turnover frequency (TOF) is calculated using the Equation (S9):[7,8]

$$TOF = \frac{F \times X}{W \times D} \quad (S9)$$

Where F is the flow rate of CO_2 at the inlet, W is the molar mass of the catalyst, D is the dispersion of the catalyst, and X is the CO_2 conversion rate to CO, which is determined from Equation (S10):

$$X = \frac{[CO_2]_{in} - [CO_2]_{out}}{[CO_2]_{in}} \times 100\% \quad (S10)$$

Table S4. Summary of parameters for Cu/ZnO catalysts at 400℃.

	ZnO	**5CuZnO**	**10CuZnO**	**20CuZnO**	**40CuZnO**	**60CuZnO**
r_0 ($\times 10^{-5}$ mol s^{-1} g^{-1})	7.90	10.2	10.9	12.9	13.7	10.9
S_{BET} (m^2 g^{-1})	10.47	23.64	30.11	36.77	39.24	25.86
TOF (s^{-1})	0.38	0.48	0.51	0.59	0.60	0.45
ρ	1.06	1.13	1.14	1.08	1.06	1.05
Λ	2.45	3.15	3.16	2.57	2.04	1.76
RF	1.00	1.22	1.45	1.17	0.86	0.58

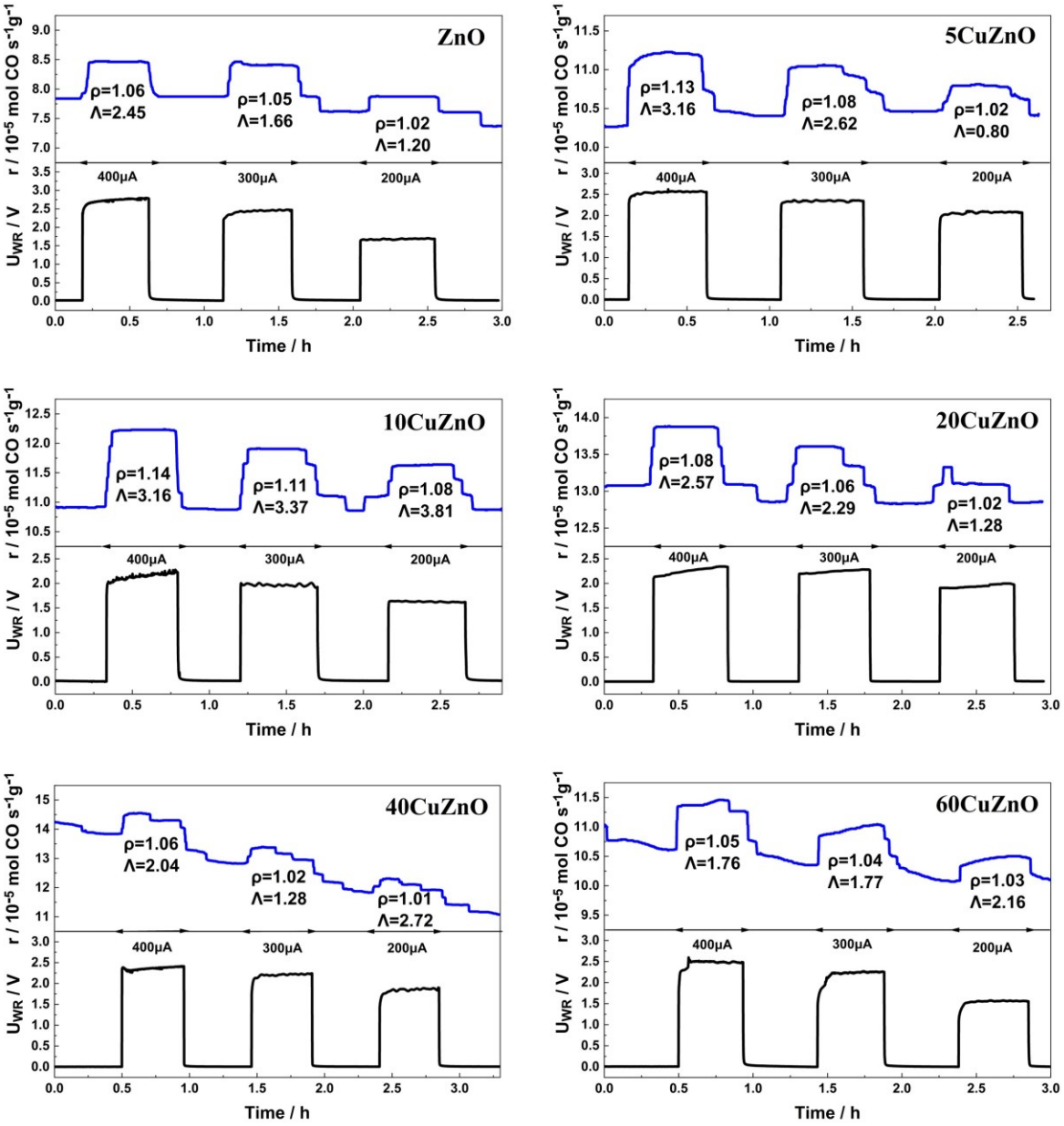

Figure S9. Overall transient responses of CO rates to applied constant currents for all Cu/ZnO catalysts under stoichiometric conditions at 400°C.

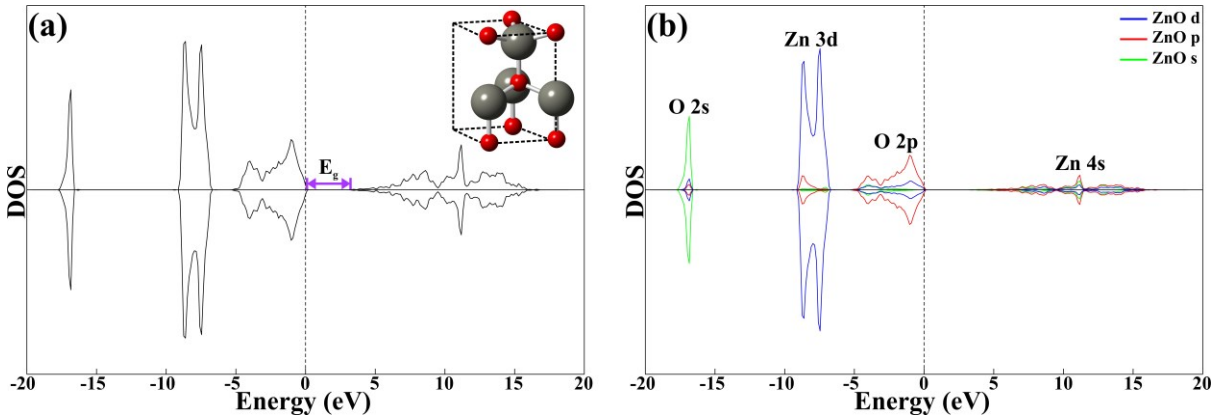

Figure S10. Total (a) and projected (b) DOS curves of wurtzite ZnO bulk. The Fermi level is the dotted line at zero. The insert represents the wurtzite ZnO unit cell, where the grey and red spheres are the Zn and O atoms, respectively.

Table S5. The adsorption sites and energies of adsorbed Cu- and O-atom on ZnO (101) surface.

	E_{ads} (eV)	
Adsorption site/ Atom	Cu	O^*
B1	-5.90	-
B2	-3.52	-
B3	-3.55	-
H1	-4.10	-0.63
H2	-0.72	-0.50
T1	-4.01	-0.49
T2	-3.53	-0.36
T3	-4.87	-0.57
T4	-3.90	-0.58
Top Cu	-	-0.54

Table S6. Bond distances for the most stable configurations.

	Distances (Å)				
System	ZnO(101)	Cu/ZnO(101)	Cu/ZnO(101) + O^*	2Cu/ZnO(101)	2Cu/ZnO(101) + O^*
Bond type					
O_1 - Zn_1	1.82	1.93	1.92	2.06	1.99
O_2 - Zn_1	1.84	1.87	1.87	1.96	1.98
O_2 - Zn_2	1.85	1.87	1.87	1.98	1.99
Cu_1 - O_1	-	1.82	1.83	1.86	1.92
Cu_1 - O_4	-	1.82	1.83	1.79	1.83
O^* - Cu_1	-	-	2.80	-	3.49
O^* - Cu_2	-	-	-	-	3.48
O^* - Zn_1	-	-	4.53	-	5.28
O^* - Zn_2	-	-	3.70	-	4.06
Cu_2 - Cu_1	-	-	-	2.59	2.45
Cu_2 - O_1	-	-	-	1.93	1.94
Cu_2 - O_2	-	-	-	1.93	1.95
Cu_2 - Zn_1	-	-	-	2.48	2.53

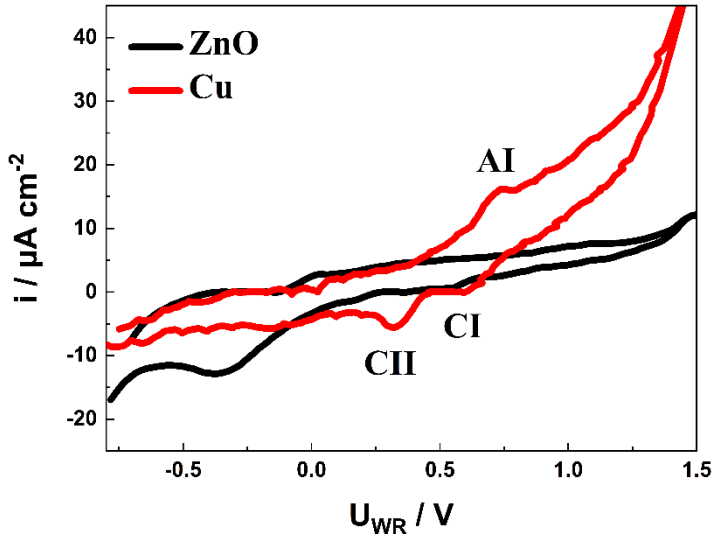

Figure S11. CVs at 400°C in Argon from -0.8 V to 1.5 V at a scan rate of 20 mV s^{-1} for unsupported Cu NPs and bare ZnO.

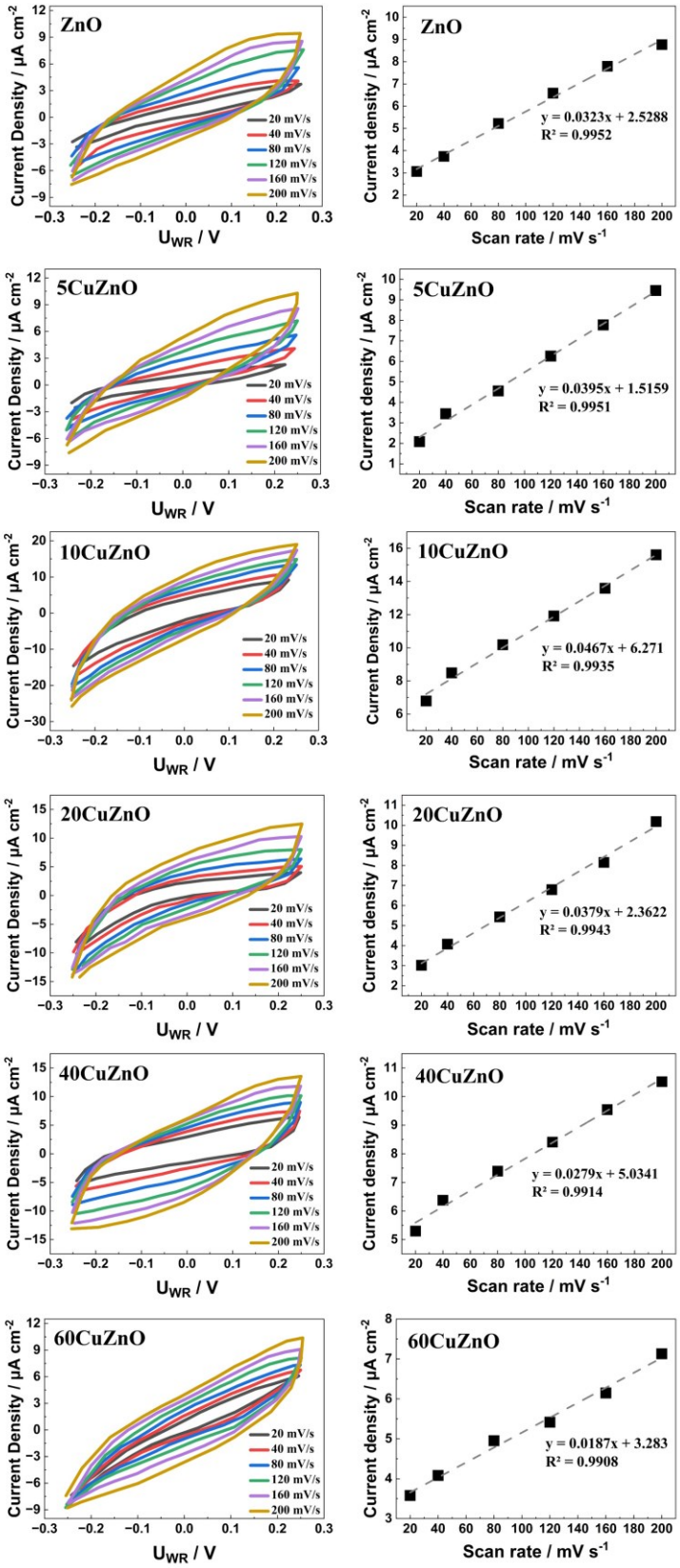

Figure S12. CVs at various scan rates and corresponding plots of current densities vs. scan rates of all Cu/ZnO catalysts for C_{dl} evaluation.

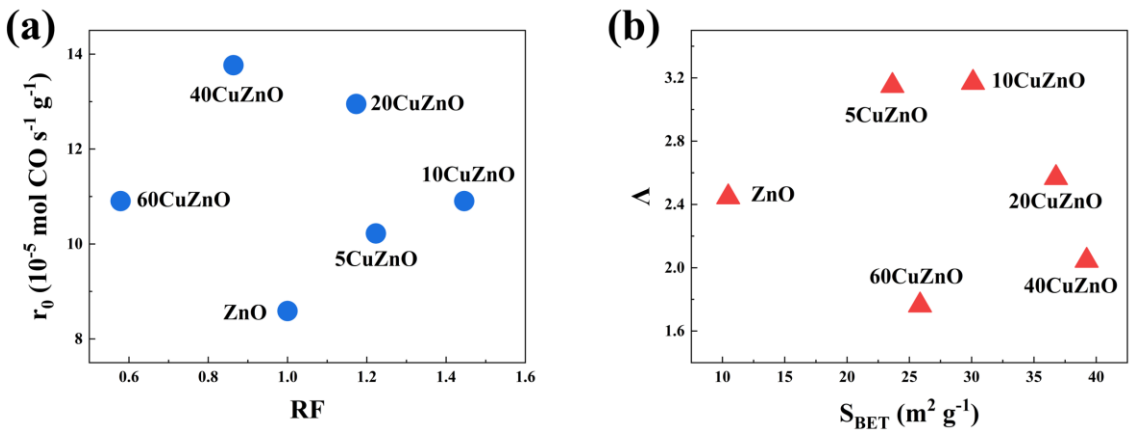

Figure S13. Relationships between (a) r_0 and RF, and (b) Λ and S_{BET} of Cu/ZnO catalysts.

References

(1) Harun, K.; Salleh, N. A.; Deghfel, B.; Yaakob, M. K.; Mohamad, A. A. DFT + U Calculations for Electronic, Structural, and Optical Properties of ZnO Wurtzite Structure: A Review. *Results Phys.* **2020**, *16* (November 2019), 102829. https://doi.org/10.1016/j.rinp.2019.102829.

(2) Karzel, H.; Potzel, W.; Köfferlein, M.; Schiessl, W.; Steiner, M.; Hiller, U.; Kalvius, G.; Mitchell, D.; Das, T. Lattice Dynamics and Hyperfine Interactions in ZnO and ZnSe at High External Pressures. *Phys. Rev. B* **1996**, *53* (17), 11425–11438. https://doi.org/10.1103/PhysRevB.53.11425.

(3) Irandegani, E.; Maezono, R.; Abbasnejad, M. Electronic and Magnetic Properties of Pure and Cu Doped Non-Polar ZnO (10 1 ¯ 0) Surfaces. *J. Appl. Phys.* **2022**, *132* (17), 0–8. https://doi.org/10.1063/5.0106799.

(4) Geng, Z.; Kong, X.; Chen, W.; Su, H.; Liu, Y.; Cai, F.; Wang, G.; Zeng, J. Oxygen Vacancies in ZnO Nanosheets Enhance CO2 Electrochemical Reduction to CO. *Angew. Chemie - Int. Ed.* **2018**, *57* (21), 6054–6059. https://doi.org/10.1002/anie.201711255.

(5) Yang, R.; Du, Y. Adsorption and Dissociation of a Single Water Molecule on Graphene-like ZnO Monolayer with Oxygen Vacancies: A First-Principles Study. *Phys. Scr.* **2023**, *98* (3). https://doi.org/10.1088/1402-4896/acba59.

(6) Bergeret, G.; Gallezot, P. Pore Size Distribution and Porosity of Solid Materials by Mercury Porosimetry and Gas Adsorption-Part 2: Analysis of Macropores by Mercury Porosimetry. *96. H. Giesche, Mater. Res. Soc. Symp. Proc* **1991**, *37* (4183), 225.

(7) Panaritis, C.; Edake, M.; Couillard, M.; Einakchi, R.; Baranova, E. A. Insight towards the Role of Ceria-Based Supports for Reverse Water Gas Shift Reaction over RuFe Nanoparticles. *J. CO2 Util.* **2018**, *26* (April), 350–358. https://doi.org/10.1016/j.jcou.2018.05.024.

(8) Ma, L.; Seo, C. Y.; Chen, X.; Li, J.; Schwank, J. W. Sodium-Promoted Ag/CeO2 Nanospheres for Catalytic Oxidation of Formaldehyde. *Chem. Eng. J.* **2018**, *350* (May), 419–428. https://doi.org/10.1016/j.cej.2018.05.179.